



Original Research Paper

Exact-solution of entropy generation for MHD nanofluid flow induced by a stretching/shrinking sheet with transpiration: Dual solution



Navid Freidoonimehr, Asghar B. Rahimi*

Faculty of Engineering, Ferdowsi University of Mashhad, P.O. Box No. 91775-1111, Mashhad, Iran

ARTICLE INFO

Article history:

Received 11 May 2016

Received in revised form 7 December 2016

Accepted 12 December 2016

Available online 27 December 2016

Keywords:

Entropy generation

Nanofluid

MHD

Stretching/shrinking sheet

Transpiration

Exact solution

Dual solution

ABSTRACT

In this article, attempts are made to present an exact solution for the fluid flow and heat transfer and also entropy generation analysis of the steady laminar magneto-hydrodynamics (MHD) nanofluid flow induced by a stretching/shrinking sheet with transpiration. This paper is the first contribution to the study of entropy generation for the nanofluid flow via exact solution approach. The governing partial differential equations are transformed into nonlinear coupled ordinary differential equations via appropriate similarity transformations. The current exact solution illustrates very good correlation with those of the previously published studies in the especial cases. The entropy generation equation is derived as a function of the velocity and the temperature gradients. The influences of the different flow physical parameters including the nanoparticle volume fraction parameter, the magnetic parameter, the mass suction/injection parameter, the stretching/shrinking parameter, and the nanoparticle types on the fluid velocity component, the temperature distribution, the skin friction coefficient, the Nusselt number and also the averaged entropy generation number are discussed in details. This study specifies that nanoparticles in the base fluid offer a potential in increasing the convective heat transfer performance of the various liquids. The results show that the copper and the aluminum oxide nanoparticles have the largest and the lowest averaged entropy generation number, respectively, among all the nanoparticles considered.

© 2016 The Society of Powder Technology Japan. Published by Elsevier B.V. and The Society of Powder Technology Japan. All rights reserved.

1. Introduction

Working fluids have great demands placed upon them in terms of increasing or decreasing energy release to systems, and their influences depend on thermal conductivity, heat capacity and other physical properties in modern thermal and manufacturing processes. A low thermal conductivity is one of the most remarkable parameters that can limit the heat transfer performance. Further, the classical heat transfer fluids such as ethylene glycol, water and engine oil have limited heat transfer capabilities due to their low thermal conductivity and thus they cannot congregate with modern cooling requirements. On the other hand, the thermal conductivity of metals is extremely higher in comparison to the conventional fluids. Suspending the ultrafine solid metallic particles in technological fluids causes a remarkable increase in the thermal conductivity. This idea is one of the most modern and appropriate methods for increasing the heat transfer coefficient. Choi and Eastman [1] were probably the first to employ a mixture of nanoparticles and base fluid which were designated as “Nanofluid”.

Experimental studies have displayed that with 1–5% volume of solid metallic or metallic oxide particles, the effective thermal conductivity of the resulting mixture can be increased by 20% compared to that of the base fluid [2–4]. One of the technological applications of nanoparticles that hold enormous promise is the use of heat transfer fluids containing suspensions of nanoparticles to confront cooling problems in the thermal systems. Xuan and Li [5] displayed the flow and heat transfer performances of nanofluids under the turbulent flow in tubes. Their experimental results showed that the convective heat transfer coefficient and the Nusselt number of nanofluids are enhanced by an increase in the Reynolds number and volume fraction of nanoparticles.

There are several investigations on nanofluids characteristics available in recent literatures. Rashidi et al. [6] studied numerically the comparison of two-phase and single phase of heat transfer and flow field of copper-water nanofluid in a wavy channel. Freidoonimehr et al. [7] investigated the transient MHD laminar free convection flow of a nanofluid past a vertical surface using four different types of water based nanofluid, numerically, via a fourth order Runge-Kutta method using a shooting technique. In another study, Freidoonimehr et al. [8] surveyed three-dimensional flow of a nanofluid in a rotating channel on a lower permeable stretching

* Corresponding author.

E-mail address: rahimiab@um.ac.ir (A.B. Rahimi).

porous wall. Further, Freidoonimehr and Rashidi [9] presented dual solutions for the problem of magneto-hydrodynamic Jeffery–Hamel nanofluid flow inside non-parallel walls using Predictor Homotopy Analysis Method (PHAM). Moreover, Freidoonimehr et al. [10] employed PHAM to solve the problem of two-dimensional nanofluid flow through expanding or contracting gaps with permeable walls considering different type of nanoparticles including silver, copper, copper oxide, titanium oxide, and aluminum oxide.

In the recent past years, the efficiency calculations of the heat exchanger systems were restricted to the first law of thermodynamics in many studies. In many industrial systems, various mechanisms that account for irreversibility compete with each other. Hereupon, thermodynamic optimization became the concern of several researchers and also it turned into the determinative condition of the most desirable trade-off between two or more competing irreversibilities, [11]. Entropy generation minimization was comprehensively covered by Bejan [12] specifically in the fields of refrigeration, heat transfer and storage, solar thermal power conversion, and thermal science education. Entropy generation minimization (EGM) method was employed to optimize the performance of thermal engineering devices for higher energy efficiency. In order to access the best practical design of thermal systems, one can employ the second law of thermodynamics to minimize the irreversibilities [13,14]. The performance of an engineering device is reduced in the presence of the irreversibilities and the entropy generation function is a measure of the level of the availability of this factor in a process. Since the entropy generation is the criteria for the measurement of the available work destruction of the systems, reduction of the entropy generation is essential to obtain the optimal design characteristics of the energy systems [15]. Moreover, entropy generation causes a decrease in the useful power cycle outputs in a power production device and an increase in the power input to the cycle for power consumption devices. It is important to emphasize that the studies based on the second law of thermodynamics are more reliable than the first law of thermodynamics analysis, because of the limitation of the first law efficiency in the heat transfer engineering systems [16]. The entropy generation analysis is done to improve the system performance. In addition, heat transfer, mass transfer, viscous dissipation, finite temperature gradients, and so on can be used as the sources of entropy generation [17].

In recent decades, many researchers were motivated to study and employ the applications of the second law of thermodynamics in the design of thermal engineering systems. Rashidi et al. [18] studied the first and second law analyzes of an electrically conducting fluid past a rotating disk in the presence of a uniform vertical magnetic field analytically and then applied Artificial Neural Network (ANN) and Particle Swarm Optimization (PSO) algorithm to minimize the entropy generation. In another study, Rashidi et al. [19] employed the second law of thermodynamics to study an electrically conducting incompressible nanofluid flowing over a porous rotating disk. Abolbashari et al. [20] employed Homotopy Analysis Method (HAM) to study an entropy analysis in an unsteady magneto-hydrodynamic nanofluid regime adjacent to an accelerating stretching permeable surface. In another study, the same authors [21] displayed an analytical investigation of the fluid flow, heat and mass transfer and entropy generation for the steady laminar non-Newtonian nanofluid flow induced by a stretching sheet in the presence of velocity slip and convective surface boundary conditions using Optimal HAM. Jafari and Freidoonimehr [22] studied the second law of thermodynamics over a stretching permeable surface in the presence of the uniform vertical magnetic field in the slip nanofluid regime. Moreover, Rashidi et al. [23] performed the study of a magnetic field with temperature-dependent thermo-physical properties numerically by using fourth-order

Runge–Kutta method. Rashidi et al. [24] studied and analyzed the convective flow of a third grade non-Newtonian fluid due to a linearly stretching sheet subject to a magnetic field by using OHAM.

The study of heat transfer in the stretched flow is of great importance because of its extensive applications in chemical engineering. Several processes in chemical engineering including the metallurgical and polymer extrusion, glass-fiber and paper production processes involve cooling of a molten liquid being stretched into a cooling system. In such processes, the rates of cooling and stretching influence the quality of the final product considerably.

The current study is mainly motivated by the need to understand the fluid flow, heat transfer and entropy generation analyses for the steady laminar MHD nanofluid flow induced by a stretching/shrinking sheet considering the transpiration effect through a surface. An exact solution is obtained for the velocity distribution and also for the temperature distribution by using the generalized Laguerre polynomial function. By achieving these exact solutions for both the velocity and temperature gradients, the entropy generation function can be obtained in exact form. Many graphs are plotted and the variations of the different involved parameters are discussed in details. The paper is divided up as follows: Section 2 describes the mathematical formula and geometric model of the problem. The exact solutions for both velocity and temperature profiles are presented in Section 3. Section 4 deals with the physical quantities of interest in this problem including the skin friction coefficient, Nusselt number and entropy generation function. Results are discussed in Section 5 and the conclusion section is presented finally.

2. Problem statement

Consider a steady MHD laminar nanofluid regime over a permeable stretching or shrinking surface in a water based incompressible nanofluid containing different type of nanoparticles, as shown in Fig. 1. It is assumed that the base fluid and the nanoparticles are in thermal equilibrium and no slip condition exists between them. It is also supposed that the magnetic Reynolds number is very small. Therefore, it is conceivable to neglect the induced magnetic field in comparison to the applied magnetic field. The flow occupies the $y > 0$ domain. The sheet is stretched in the x -direction by keeping the origin as fixed. The velocity of the sheet along the x -direction is equal to $u_w(x) = bx$. The velocity of the mass transfer perpendicular to the stretching surface is presented by v_w . The temperature of the surface, $T_w(x)$, varies linearly by x while the temperature of the ambient fluid is represented by T_∞ . The basic steady 2-D conservation of mass, momentum and thermal energy equations for the nanofluid is written as the following by using the above assumptions and applying the Boussinesq and boundary-layer approximations for negligible viscous dissipation:

$$\frac{\partial u}{\partial x} + \frac{\partial v}{\partial y} = 0, \quad (1)$$

$$\rho_{nf} \left(u \frac{\partial u}{\partial x} + v \frac{\partial u}{\partial y} \right) = \mu_{nf} \frac{\partial^2 u}{\partial y^2} - \sigma B_0^2 u, \quad (2)$$

$$(\rho c_p)_{nf} \left(u \frac{\partial T}{\partial x} + v \frac{\partial T}{\partial y} \right) = k_{nf} \frac{\partial^2 T}{\partial y^2}, \quad (3)$$

where u and v are the velocity components in the x and y directions, respectively, ρ_{nf} and μ_{nf} are the density and the dynamic viscosity of the nanofluid, respectively, where μ_{nf} has been proposed by Brinkman [25], T is the nanofluid temperature, σ is the electrical conductivity, B_0 is the magnetic field imposed along the y -axis, $(\rho c_p)_{nf}$ is the heat capacitance of the nanofluid and k_{nf} is the

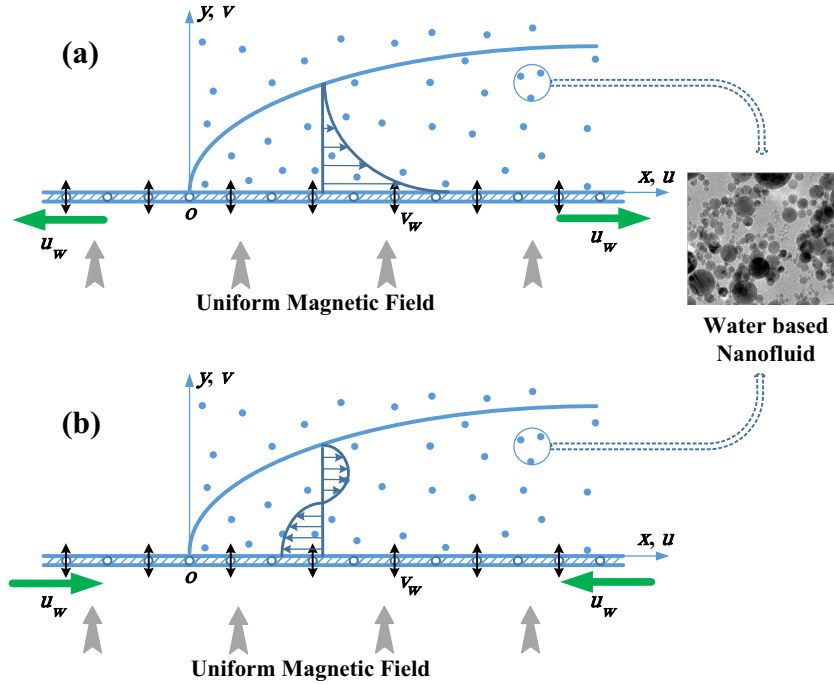


Fig. 1. Schematic diagram of physical model and coordinate system (a) Stretching sheet ($\lambda > 0$) and (b) Shrinking sheet ($\lambda < 0$).

effective thermal conductivity of the nanofluid [26]. These nanofluid constants are defined by:

$$\begin{aligned}
 (\rho c_p)_{nf} &= (1 - \varphi)(\rho c_p)_f + \varphi(\rho c_p)_s, \\
 \rho_{nf} &= (1 - \varphi)\rho_f + \varphi\rho_s, \quad \frac{k_{nf}}{k_f} = \frac{(k_s + 2k_f) - 2\varphi(k_f - k_s)}{(k_s + 2k_f) + \varphi(k_f - k_s)}, \\
 \mu_{nf} &= \frac{\mu_f}{(1 - \varphi)^{2.5}},
 \end{aligned}
 \tag{4}$$

where φ is the nanoparticle volume fraction parameter and the subscripts f and s refer to the fluid and solid fraction properties, respectively. It should be mentioned that the use of the approximation for k_{nf} is restricted to the spherical nanoparticles and does not account for other nanoparticle shapes. The thermophysical properties of the base fluid (water) and different nanoparticles are given in Table 1, [26,27].

Boundary conditions are:

$$\begin{aligned}
 u &= u_w(x) = bx, \quad v = v_w, \quad T = T_w(x) = T_\infty + ax, \quad \text{at } y = 0, \\
 u &\rightarrow 0, \quad T \rightarrow T_\infty, \quad \text{as } y \rightarrow \infty,
 \end{aligned}
 \tag{5}$$

where a and b are constants ($a > 0$). The following dimensionless functions $f(\eta)$ and $\theta(\eta)$, and the appropriate similarity variables are employed as:

$$\eta = \left(\frac{a}{v_f}\right)^{1/2} y, \quad \psi(x, y) = (v_f a)^{1/2} x f(\eta), \quad \theta(\eta) = \frac{T - T_\infty}{T_w - T_\infty}, \tag{6}$$

where $\psi(x, y)$ is the free-stream function that satisfies the continuity equation as:

$$u = \frac{\partial \psi}{\partial y} = axf'(\eta), \quad v = -\frac{\partial \psi}{\partial x} = -(v_f a)^{1/2} f(\eta). \tag{7}$$

The following ordinary differential equations are obtained by substituting the variables (6) and (7) into the Eqs. (2)–(3) and (5):

$$\frac{1}{(1 - \varphi)^{2.5}} f'''(\eta) - \left(1 - \varphi + \varphi \left(\frac{\rho_s}{\rho_f}\right)\right) [f'^2(\eta) - f(\eta)f''(\eta)] - Mf'(\eta) = 0, \tag{8}$$

$$\frac{k_{nf}/k_f}{1 - \varphi + \varphi \left(\frac{\rho c_p}_s / (\rho c_p)_f\right)} \theta''(\eta) + Pr(f(\eta)\theta'(\eta) - f'(\eta)\theta(\eta)) = 0, \tag{9}$$

The transformed boundary conditions become:

$$\begin{aligned}
 f(\eta) &= f_w, \quad f'(\eta) = \lambda, \quad \theta(\eta) = 1, \quad \text{at } \eta = 0, \quad f'(\eta) \rightarrow 0, \\
 \theta(\eta) &\rightarrow 0, \quad \text{as } \eta \rightarrow \infty,
 \end{aligned}
 \tag{10}$$

where prime denotes differentiation with respect to η , $M = \sigma B_0^2 / a \rho_f$ is the magnetic parameter, $Pr = v_f / \alpha_f$ is the Prandtl number, $f_w (= -v_w / \sqrt{v_f a})$ is the mass suction/injection parameter, and $\lambda = b/a$ is the stretching/shrinking parameter.

3. Problem solution

3.1. Solution of the flow field

Now we seek the solution of Eq. (8) in the form of

$$f(\eta) = a + be^{-\alpha \eta} \quad (\alpha > 0), \tag{11}$$

Table 1
Thermo-physical properties of the base fluid and different nanoparticles.

Physical properties	Fluid phase (water)	Cu	CuO	Al ₂ O ₃	TiO ₂
c_p (J/kg K)	4076.4	385	531.8	765	686.2
ρ (kg/m ³)	997.8	8933	6320	3970	4250
k (W/m K)	0.60475	401	76.5	40	8.9538

where the above equation is satisfied by the following boundary conditions:

$$f(0) = f_w, \quad f'(0) = \lambda, \quad f'(\infty) = 0, \tag{12}$$

By substituting Eq. (11) into the Eqs. (8) and (12) yields:

$$a = f_w + \frac{\lambda}{\alpha}, \quad b = -\frac{\lambda}{\alpha}, \tag{13}$$

where α satisfies the following equation:

$$\frac{\lambda}{(1-\varphi)^{5/2}} \alpha^2 - \left(1 - \varphi + \varphi \left(\frac{\rho_s}{\rho_f}\right)\right) (f_w \lambda \alpha + \lambda^2) - M \lambda = 0, \tag{14}$$

By solving this equation, the value of α is obtained as:

$$\alpha = \frac{1}{2} \left(f_w \left(1 - \varphi + \varphi \left(\frac{\rho_s}{\rho_f}\right)\right) (1 - \varphi)^{2.5} \pm \sqrt{4 \left(M + \lambda \left(1 - \varphi + \varphi \left(\frac{\rho_s}{\rho_f}\right)\right)\right) \sqrt{1 - \varphi} - f_w^2 \left(1 - \varphi + \varphi \left(\frac{\rho_s}{\rho_f}\right)\right)^2 (-1 + \varphi)^3 (-1 + \varphi)^2} \right), \tag{15}$$

Thus, the exact solution of Eq. (8) subject to the corresponding boundary conditions is given by

$$f(\eta) = f_w + \frac{\lambda}{\alpha} (1 - e^{-\alpha \eta}), \tag{16}$$

The velocity profile for both the stretching and shrinking surfaces is determined after differentiating Eq. (16) as:

$$f'(\eta) = \lambda e^{-\alpha \eta}, \tag{17}$$

The solution domain for this problem is determined by the mass suction/injection parameter, stretching/shrinking parameter, magnetic parameter, and nanoparticle volume fraction parameter as shown in Figs. 2 and 3. In order to have a physical solution, α must be greater than zero.

3.2. Solution of the temperature field

Having determined $f(\eta)$ in (16) and by using the intermediate variable

$$\zeta = -e^{-\alpha \eta}, \tag{18}$$

The energy Eq. (9) can be written as the subsequent linear second-order boundary value problem with variable coefficients

$$\zeta \theta''(\zeta) + \left(1 - \frac{p}{pnc} - \frac{Pr^* \lambda}{pnc} \zeta\right) \theta'(\zeta) + \frac{Pr^* \lambda}{pnc} \theta(\zeta) = 0, \tag{19}$$

Subject to the following boundary conditions:

$$\theta(-1) = 1, \quad \theta(0) = 0, \tag{20}$$

where

$$pnc = \frac{k_{nf}/k_f}{1 - \varphi + \varphi((\rho c_p)_s/(\rho c_p)_f)}, \quad p = Pr^*(\lambda + f_w \alpha), \quad \text{and} \quad Pr^* = \frac{Pr}{\alpha^2}$$

The solution of Eq. (19) obtained in terms of Laguerre polynomials by considering the boundary conditions Eq. (20) as, [28,29]:

$$\theta(\zeta) = \frac{(-1)^{-\frac{p}{pnc}} \zeta^{\frac{p}{pnc}} L \left[1 - \frac{p}{pnc}, \frac{p}{pnc}, \frac{Pr^* \lambda}{pnc} \zeta \right]}{L \left[1 - \frac{p}{pnc}, \frac{p}{pnc}, -\frac{Pr^* \lambda}{pnc} \right]}, \tag{21}$$

where $L[a, b, z]$ is the generalized Laguerre Polynomial.

4. Parameters of engineering interest

4.1. Skin friction coefficient

The skin friction coefficient, as one of the most important physical quantities, along the x direction is defined as follows:

$$C_{fx} = \frac{\tau_w}{\rho_f U_w^2}, \tag{22}$$

where τ_w is the surface shear-stress and is given by:

$$\tau_w = \mu_{nf} \left. \frac{\partial u}{\partial y} \right|_{y=0}, \tag{23}$$

The dimensionless skin friction coefficient is obtained by applying the non-dimensional transformations (6) and (7):

$$C_{fx} Re_x^{1/2} = \frac{1}{(1-\varphi)^{2.5}} f''(0), \tag{24}$$

where $Re_x = u_w x / \nu_f$ is the local Reynolds number. Finally, according to the Eq. (16), the dimensionless exact skin friction coefficient is obtained as:

$$C_{fx} Re_x^{1/2} = -\frac{1}{(1-\varphi)^{2.5}} \alpha \lambda, \tag{25}$$

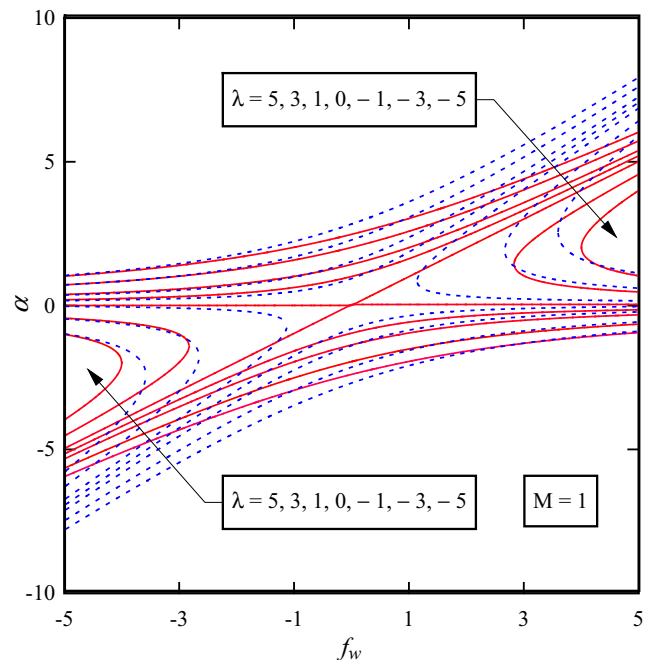


Fig. 2. The solution domain for α at different values of stretching/shrinking parameter (λ) as a function of the mass suction/injection parameter (f_w); red solid line and blue dotted line correspond to the $\varphi = 0$, and $\varphi = 0.1$, respectively. (For interpretation of the references to colour in this figure legend, the reader is referred to the web version of this article.)

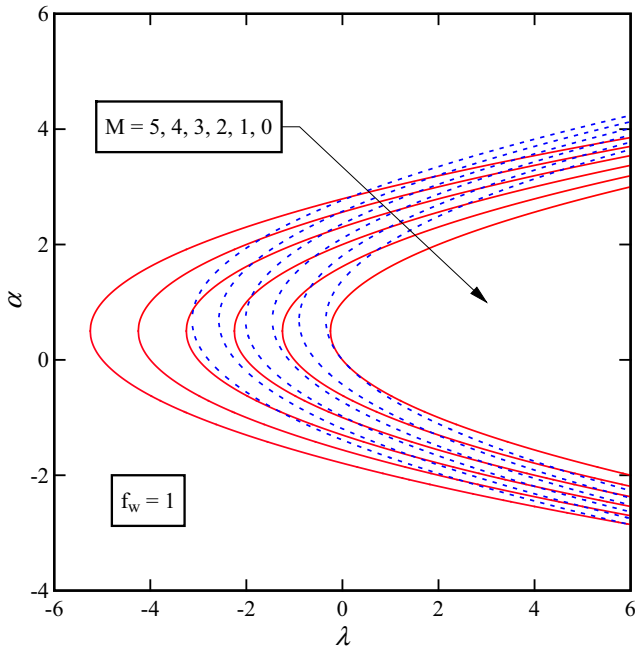


Fig. 3. The solution domain for α at different values of magnetic parameter (M) as a function of the stretching/shrinking parameter (λ); red solid line and blue dotted line correspond to $\varphi = 0$ and $\varphi = 0.1$, respectively. (For interpretation of the references to colour in this figure legend, the reader is referred to the web version of this article.)

4.2. Nusselt number

The other important physical quantity, the local Nusselt number (Nu_x), is given by:

$$Nu_x = \frac{xq_w}{k_f(T_f - T_\infty)}, \tag{26}$$

where q_w is the surface heat flux introduced as,

$$q_w = -k_{nf} \left(\frac{\partial T}{\partial y} \right)_{y=0}, \tag{27}$$

Applying the non-dimensional transformations (6) and (7), one obtains

$$Nu_x/Re_x^{1/2} = -\frac{k_{nf}}{k_f} \theta'(0), \tag{28}$$

Therefore, based on the Eq. (21), the dimensionless Nusselt number is obtained as:

$$Nu_x/Re_x^{1/2} = \frac{k_{nf}}{k_f} \left(\frac{\alpha p}{pnc} + \frac{Pr^* \alpha \lambda L \left[-\frac{p}{pnc}, 1 + \frac{p}{pnc}, -\frac{Pr^* \lambda}{pnc} \right]}{pnc L \left[1 - \frac{p}{pnc}, \frac{p}{pnc}, -\frac{Pr^* \lambda}{pnc} \right]} \right), \tag{29}$$

4.3. Entropy generation analysis

According to [12,20], the volumetric rate of the local entropy generation of the nanofluid flow in the presence of a magnetic field effect over the stretching/shrinking surface can be described as:

$$\dot{S}_{gen}''' = \underbrace{\frac{k_{nf}}{T_\infty^2} \left[\left(\frac{\partial T}{\partial x} \right)^2 + \left(\frac{\partial T}{\partial y} \right)^2 \right]}_{\text{Heat Transfer Irreversibility}} + \underbrace{\frac{\mu_{nf}}{T_\infty} \left(\frac{\partial u}{\partial y} \right)^2}_{\text{Fluid Friction Irreversibility}} + \underbrace{\frac{\sigma B_0^2}{T_\infty} u^2}_{\text{Joule Dissipation Irreversibility}}, \tag{30}$$

Eq. (30) reveals that the entropy generation is due to three effects: the first effect, a conduction effect, is the entropy generation due to heat transfer across a finite temperature difference. The second effect is due to the fluid friction irreversibility and the last effect denotes the magnetic effects in the form of joule dissipation irreversibilities which are caused by the movement of an electrically conducting fluid under the effect of the magnetic field. The entropy generation number (N_G), dimensionless form of the entropy generation rate, represents the ratio between the actual entropy generation rate (\dot{S}_{gen}''') and the characteristic entropy generation rate (\dot{S}_0'''). In order to non-dimensionalize the local entropy generation, the similarity transformation parameters in Eqs. (6) and (7) are employed. Thus, the entropy generation number becomes:

$$N_G = \frac{k_{nf}}{k_f} \left(\frac{\Omega}{X^2} (\theta(\eta))^2 + \frac{\Omega Re_L}{\lambda} (\theta'(\eta))^2 \right) + \frac{\mu_{nf}}{\mu_f} \frac{Br Re_L}{\lambda^3} (f''(\eta))^2 + \frac{Br Ha^2}{\lambda^2} (f'(\eta))^2, \tag{31}$$

where $\dot{S}_0''' = k_f \Delta T / L^2 T_\infty$ is the characteristic entropy generation rate, $X = x/L$ is the dimensionless distance in the x -direction, $Re_L = bL^2 / \nu_f$ is the Reynolds number, $Br = \mu_f u_w^2 / k_f \Delta T$ is the Brinkman number which represents the ratio of direct heat conduction from the surface to the viscous heat generated by shear in the boundary-layer, $Ha = B_0 L \sqrt{\sigma / \mu_f}$ is the Hartmann number, and $\Omega = \Delta T / T_\infty$ is the dimensionless temperature difference.

Substituting the obtained exact solutions of the velocity (Eq. (16)) and the temperature (Eq. (21)) fields in the relation for entropy generation number of Eq. (31), the exact form of the entropy generation number is obtained as:

$$N_G = \frac{k_{nf}}{k_f} \left(\frac{\Omega}{X^2} \left(\frac{(-1)^{-\frac{p}{pnc}} (-e^{-\alpha \eta})^{\frac{p}{pnc}} L \left[1 - \frac{p}{pnc}, \frac{p}{pnc}, -\frac{Pr^* \lambda}{pnc} e^{-\alpha \eta} \right]}{L \left[1 - \frac{p}{pnc}, \frac{p}{pnc}, -\frac{Pr^* \lambda}{pnc} \right]} \right)^2 + \frac{\Omega Re_L}{\lambda} \times \left(\frac{\alpha}{pnc} \frac{(-1)^{-\frac{p}{pnc}} (-e^{-\alpha \eta})^{\frac{p}{pnc}+1}}{L \left[1 - \frac{p}{pnc}, \frac{p}{pnc}, -\frac{Pr^* \lambda}{pnc} \right]} \left(p e^{\alpha \eta} L \left[1 - \frac{p}{pnc}, \frac{p}{pnc}, -\frac{Pr^* \lambda}{pnc} e^{-\alpha \eta} \right] + Pr^* \lambda L \left[-\frac{p}{pnc}, 1 + \frac{p}{pnc}, -\frac{Pr^* \lambda}{pnc} e^{-\alpha \eta} \right] \right)^2 \right) + \frac{\mu_{nf}}{\mu_f} \frac{Br Re_L}{\lambda^3} (-\alpha \lambda e^{-\alpha \eta})^2 + \frac{Br Ha^2}{\lambda^2} (\lambda e^{-\alpha \eta})^2, \tag{32}$$

The dimensionless volumetric entropy generation rate, an important measure of the total global entropy generation, can be evaluated by using the following formula:

$$N_{G,av} = \frac{1}{\nabla} \int_0^m \int_0^1 N_G dX d\eta, \tag{33}$$

In which, ∇ is the volume being considered here. In order to consider both the velocity and thermal boundary-layers, we calculate the volumetric entropy generation in a large finite domain range of $0 \leq X \leq 1$ and $0 \leq \eta \leq m$, where m is a sufficiently large number.

5. Results and discussions

The nonlinear ordinary differential Eqs. (8) and (9) subject to the boundary conditions (10) are solved exactly via introducing a close form solution for the velocity field as well as using the generalized Laguerre polynomial function for the temperature distribution for some values of the nanoparticle volume fraction parameter (φ), magnetic parameter (M), stretching/shrinking

parameter (λ), and mass suction/injection parameter (f_w). In this analysis, four types of nanoparticles; Copper (Cu), copper oxide (CuO), aluminum oxide (Al_2O_3), and titanium dioxide (TiO_2) with water as the base fluid are considered. The copper nanoparticle is used in all figures in this section except those focusing on the influence of the type of applied nanoparticles on the engineering parameters such as the skin friction coefficient, the local Nusselt number and the averaged entropy generation function. For the pre-

5.1. Stretching-sheet case

For the MHD flow of Newtonian fluid and based on the above explanations, the exact solution exists in the stretching-sheet case by using Eqs. (16) and (21). It is obvious from Figs. 2 and 3 that in the stretching-sheet case, ($\lambda > 0$), only one close form solution exists. Therefore, the acceptable form of α in this case is obtained as:

$$\alpha = \frac{1}{2} \left(f_w \left(1 - \varphi + \varphi \left(\frac{\rho_s}{\rho_f} \right) \right) (1 - \varphi)^{2.5} + \sqrt{ \left(4 \left(M + \lambda \left(1 - \varphi + \varphi \left(\frac{\rho_s}{\rho_f} \right) \right) \right) \sqrt{1 - \varphi} - f_w^2 \left(1 - \varphi + \varphi \left(\frac{\rho_s}{\rho_f} \right) \right)^2 (-1 + \varphi)^3 \right) (-1 + \varphi)^2 } \right), \quad (34)$$

sent investigation, the value of the Prandtl number (Pr) is considered to be equal to 6.587 (for water at 20 °C) [27]. As explained in the previous section, a close form solution exists in both stretching and shrinking sheet cases under different conditions. For validating the present analytical results, we have performed the comparisons in case of stretching sheet for $-f''(0)$ values with Turkiylmazoglu results [30] when $\varphi = 0$, $f_w = 2$ and $\lambda = 1$ and $-\theta'(0)$ also with Abolbashari et al. results [20] when $\varphi = M = f_w = 0$ and $\lambda = 1$. These comparisons can be found in Tables 2 and 3, respectively. As it can be seen in these tables, results are in a good agreement with the above-mentioned references. Tables 3 and 4 represent the values of $f''(0)$ and $\theta'(0)$ for the different values of mass suction/injection and nanoparticle volume fraction parameters for both the stretching and shrinking sheet cases. It is obvious that dual solutions exist in the shrinking sheet case and both the solution branches (the lower branch is presented in brackets) are depicted in Table 3 (see Table 5).

The effect of nanoparticle volume fraction parameter on the velocity profile and the temperature distribution for the stretching sheet case ($\lambda = 1$) is shown in Fig. 4. In the current analysis, the value of the nanoparticle volume fraction parameter (φ) varies from 0 (regular Newtonian fluid) to 0.2. The results represent that the velocity profile decreases as the value of the nanoparticle volume fraction parameter increases. This happens because of the presence of the solid nanoparticles that leads to further thinning of the velocity boundary-layer thickness. In addition, the thermal conductivity enhances and consequently the thermal boundary-layer thickness increases as the nanoparticle volume fraction parameter increases. This issue is in compliance with the primary proposes of employing nanofluid. This also agrees with the physical behavior that when the volume of nanoparticles enhances the thermal conductivity increases and then the thermal boundary layer thickness increases.

The effect of magnetic parameter on the velocity profile and the temperature distribution for $\lambda = 1$ is demonstrated in Fig. 5. A drag-like force called Lorentz force is created by the inflection of the vertical magnetic field to the electrically conducting fluid. This force has the tendency to slow down the movement of the fluid over the stretching surface which leads to a decrease in the velocity and the momentum boundary layer thickness. This clearly demonstrates that the transverse magnetic field opposes the transport phenomena. It is also important to mention that a greater resistance on the nanofluid particles is applied as the vertical magnetic field increases. This causes heat to be generated in the fluid.

Table 2
Comparison for $-f''(0)$ results between the present work and Ref. [30] for case $\varphi = 0$, $f_w = 2$ and $\lambda = 1$.

M	Present result	Turkiylmazoglu (Ref. [30])
0	2.39871456	2.41421356
2	2.98555535	3.00000000
5	3.61168892	3.64575131

Table 5
Values of $\theta'(0)$ for different values of the mass suction/injection and the nanoparticle volume fraction parameters for stretching sheet case when $M = 3$ and $\lambda = 1$.

f_w	$\varphi = 0$	$\varphi = 0.1$	$\varphi = 0.2$
-2	-0.45707795	-0.45410574	-0.44844926
-1	-0.80928202	-0.78274855	-0.75220147
0	-2.71586672	-2.28266995	-1.94479244
1	-7.82650853	-5.97050252	-4.64277038
2	-13.9327461	-10.42169178	-7.93184327

Table 3
Comparison results of $-\theta'(0)$ for different value of Prandtl number (Pr) when $\varphi = M = f_w = 0$ and $\lambda = 1$.

Pr	Present result	Abolbashari et al. (Ref. [20])
0.72	0.80863135	0.80863135
1.00	1.00000000	1.00000000
3.00	1.92368259	1.92368259
7.00	3.07225021	3.07225021
10.0	3.72067390	3.72067390

Table 4
Values of $f''(0)$ for different values of the mass suction/injection and the nanoparticle volume fraction parameters for both the stretching and shrinking sheet cases when $M = 3$.

f_w	Stretching sheet case ($\lambda = 1$)			Shrinking sheet case ($\lambda = -1$)		
	$\varphi = 0$	$\varphi = 0.1$	$\varphi = 0.2$	$\varphi = 0$	$\varphi = 0.1$	$\varphi = 0.2$
-2	-1.23606798	-0.98434789	-0.84071464	0.73205081 [-2.73205081]	0.30238824 [-3.06147873]	0.07702940 [-3.04285172]
-1	-1.56155281	-1.34999009	-1.19502776	1 [-2]	0.49409453 [-1.87363978]	0.14406428 [-1.62697544]
0	-2	-1.91959518	-1.78891346	1.41421356 [-1.41421356]	0.96216172 [-0.96216172]	0.48413742 [-0.48413742]
1	-2.56155281	-2.72953534	-2.67793892	2 [-1]	1.87363978 [-0.49409453]	1.62697544 [-0.14406428]
2	-3.23606798	-3.74343838	-3.80653696	2.73205081 [-0.73205081]	3.06147873 [-0.30238824]	3.04285172 [-0.07702940]

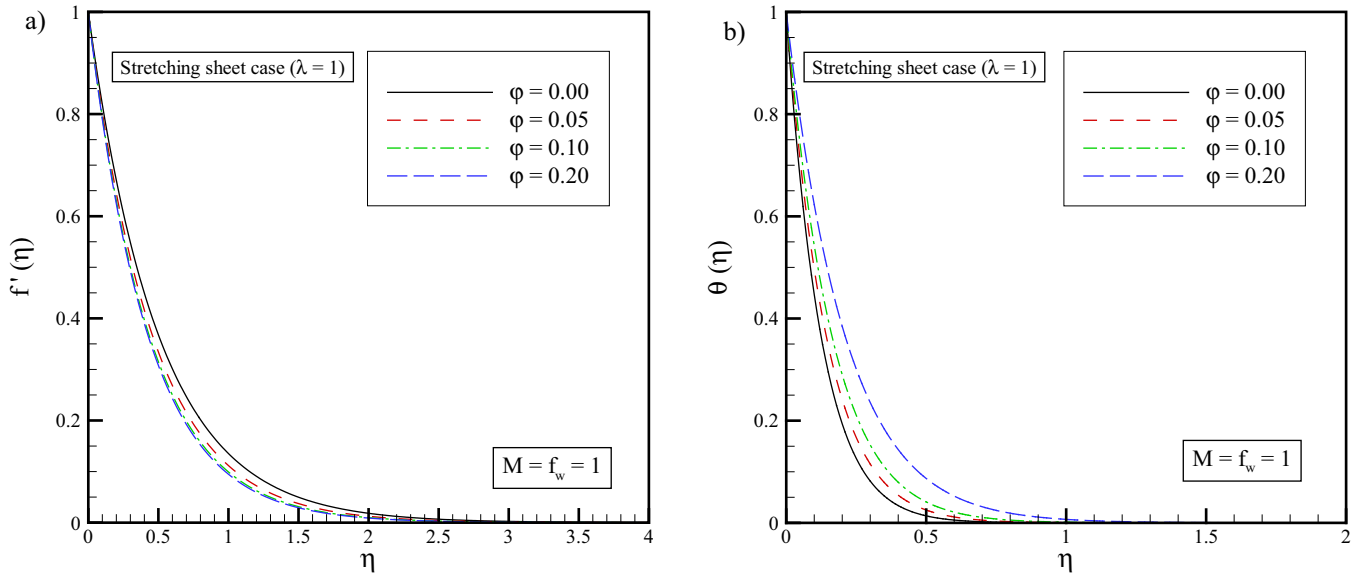


Fig. 4. Effect of the nanoparticle volume fraction parameter on (a) the velocity profile and (b) the temperature distribution.

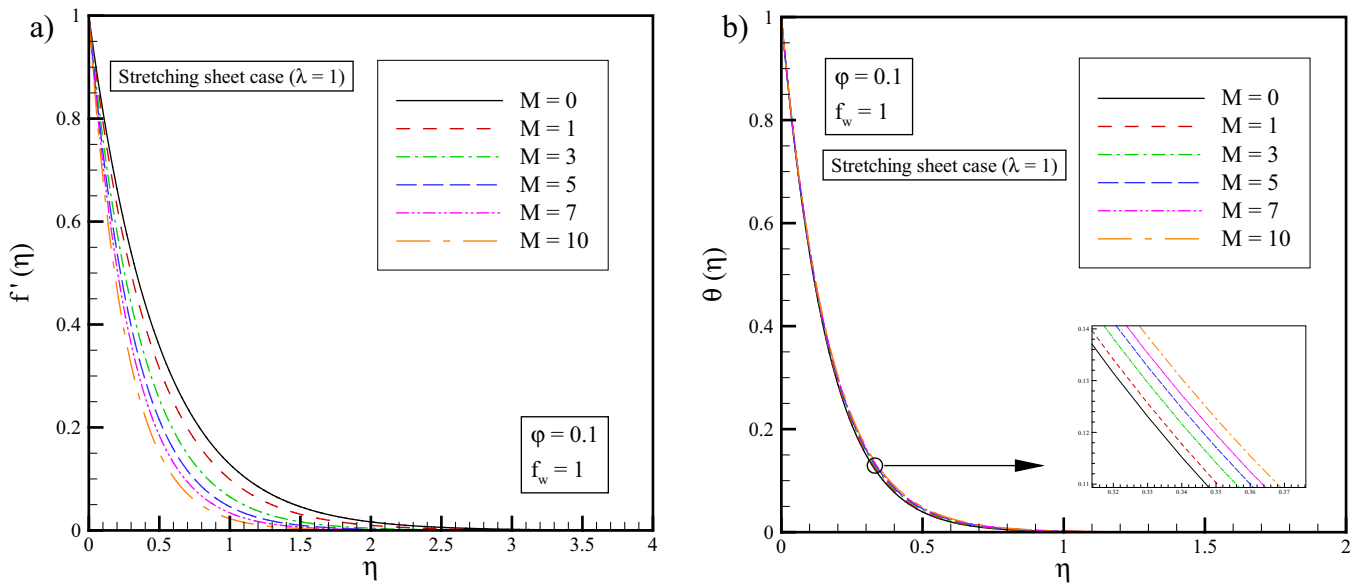


Fig. 5. Effect of the magnetic parameter on (a) the velocity profile and (b) the temperature distribution.

In other words, the temperature distribution increases slightly with an increase in the magnetic parameter.

The effect of the mass suction/injection parameter on the velocity profile and the temperature distribution is shown in Fig. 6. As it is clear by the definition of the mass suction/injection parameter, ($f_w = -v_w/\sqrt{\nu_f a}$), three different cases can be considered: (a) $f_w < 0$ corresponds to the mass injection case, (b) $f_w = 0$ refers to the wall without permeability, and (c) $f_w > 0$ denotes to the mass suction case. Applying suction through the stretching-sheet, draws a certain amounts of fluid into the surface and consequently the hydrodynamic boundary-layer gets thinner and also the thermal boundary-layer gets depressed by increasing the mass suction parameter. On the other hand, the opposite trend takes place for the mass injection case. Mass injection through the stretching-sheet causes more fluid to be injected to the surface and then the hydrodynamic

boundary-layer enhances and the value of the temperature distribution increases as well.

The effect of the stretching/shrinking parameter on the velocity profile and the temperature distribution for the stretching-sheet cases is demonstrated in Fig. 7. The initiated value of the velocity profile completely depends on the stretching/shrinking parameter, which satisfies the conditions on the bounding surface. As it is expected, the velocity distribution increases as a consequence of an increase in the stretching/shrinking parameter. In addition, the thickness of the thermal boundary layer reduces by increasing the velocity rate of the stretching sheet.

5.2. Shrinking-sheet case

The shrinking-sheet flow is more interesting than the stretching-sheet flow. The dual solutions existed in the

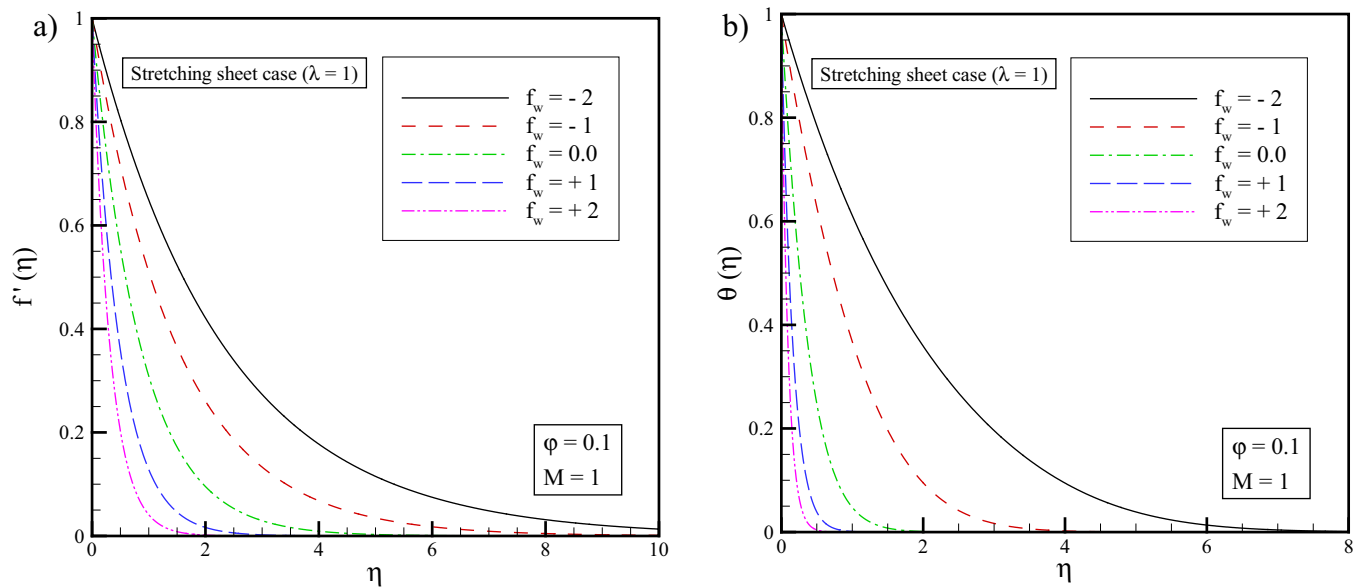


Fig. 6. Effect of the mass suction/injection parameter on (a) the velocity profile and (b) the temperature distribution.

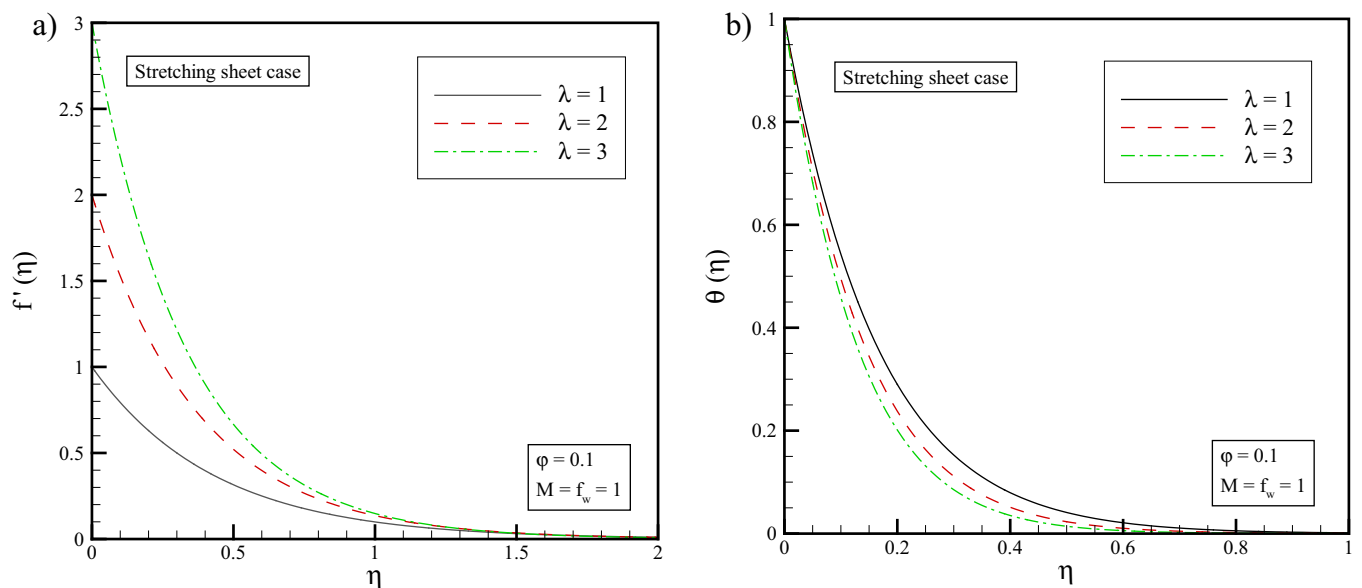


Fig. 7. Effect of the stretching/shrinking parameter on (a) the velocity profile and (b) the temperature distribution.

shrinking-sheet case for some specific values of the governing parameters are depicted in Figs. 2 and 3. There are two solution branches corresponding to the “+” and “–” sign in Eq. (15) and a dual solution exists only for the mass suction case. The conditions that two solution branches are existed depend on two factors: (a) the positive sign of α and (b) the positive sign of the term under the square root sign in α .

The effect of the nanoparticle volume fraction parameter on the velocity profile and the temperature distribution for the shrinking-sheet case is displayed in Fig. 8. The obtained results present the same trend with the stretching-sheet case as shown in Fig. 4 but with one difference which is the existence of a dual solution in the shrinking-sheet case. The hydrodynamics velocity boundary

layer decreases and the thermal boundary layer enhances by increasing in the value of the nanoparticle volume fraction parameter. It is clear that the lower solution branch for velocity and temperature profiles exhibit a larger boundary layer thickness compared with the upper solution branches. The effect of the magnetic parameter on the velocity and the temperature distributions for the shrinking-sheet case, ($\lambda < 0$), is illustrated in Fig. 9. Increasing the magnetic parameter value causes the thicknesses of the hydrodynamics velocity and the thermal boundary layers to be decreased (for the upper solution branch). In other word, it is seen that horizontal velocity at a point increases with increase in M for the upper (first) solution and the opposite is true for the lower (second) solution. In addition, Fig. 9(b) reveals that the tempera-

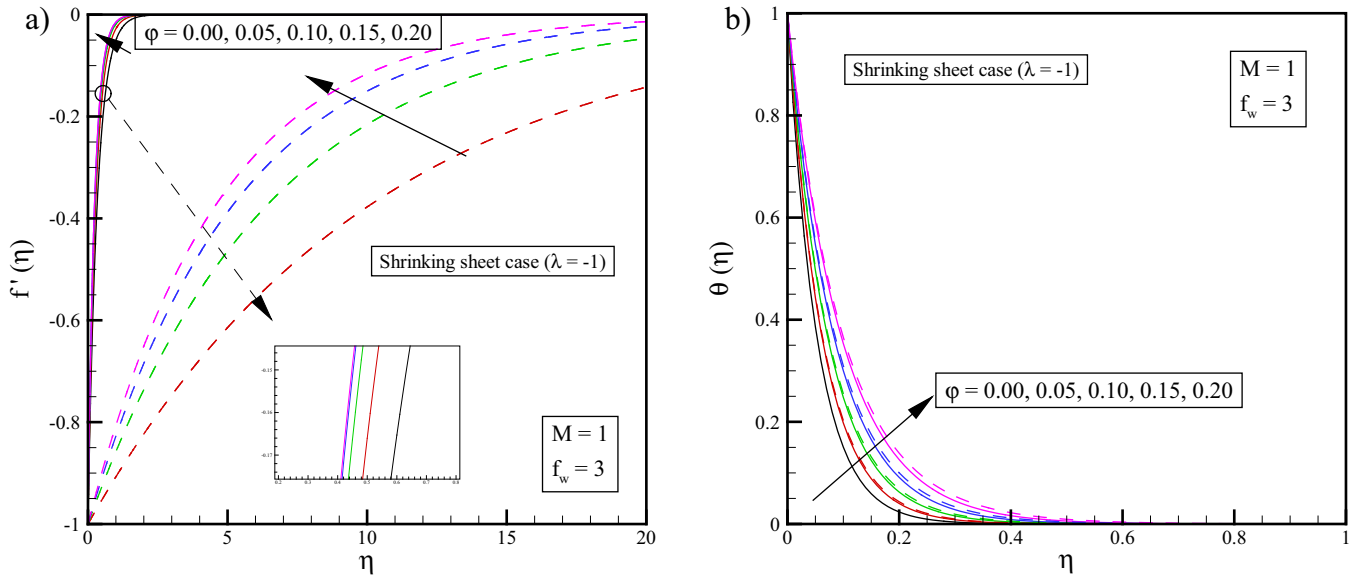


Fig. 8. Effect of the nanoparticle volume fraction parameter on (a) the velocity profile and (b) the temperature distribution; the solid line corresponds to the upper branch solution and the dashed line denotes to the lower branch solution.

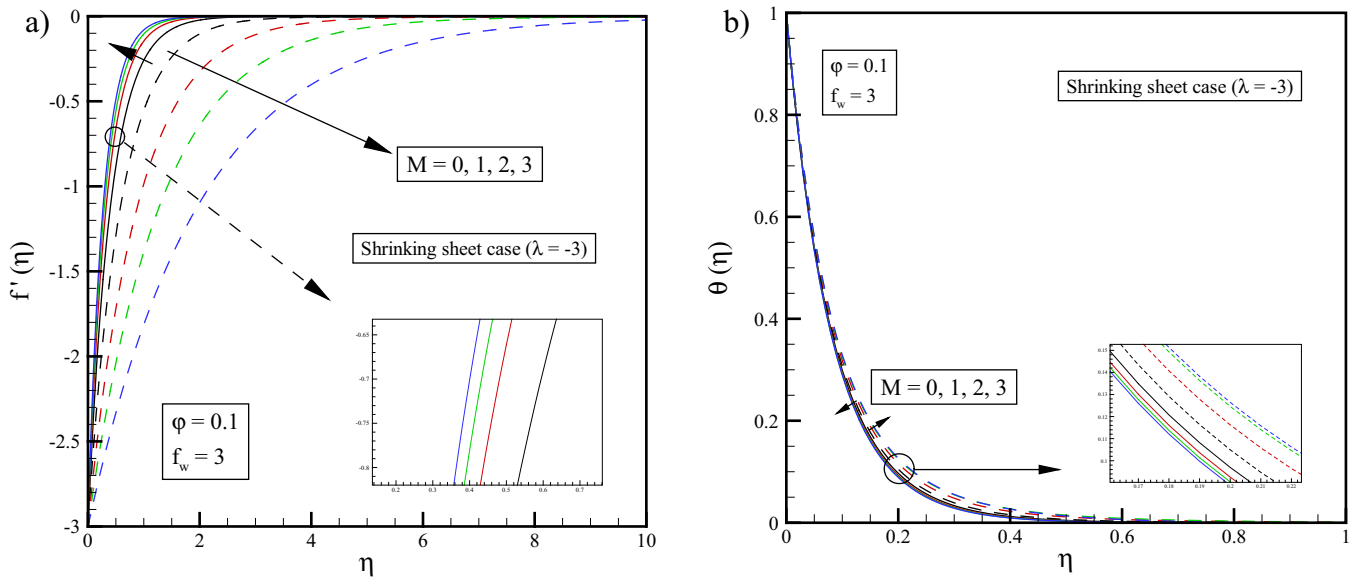


Fig. 9. Effect of the magnetic parameter on (a) the velocity profile and (b) the temperature distribution; the solid line corresponds to the upper branch solution and the dashed line denotes to the lower branch solution.

ture at a point decreases with increase in M except in a small region near the sheet for the first solution and increases with increase in M for the second solution. Physically, this can be explained as follows. The extent of the reverse cellular flow above the sheet decreases with increase in M and consequently the temperature field is influenced by the advection of the fluid velocity above the sheet.

The effect of the mass suction/injection parameter on both the velocity and the temperature profiles for the shrinking-sheet case is depicted in Fig. 10. The same trend is observed in this case as well. Both the velocity and the thermal boundary layers decrease by increasing the mass suction/injection parameter in the suction case. In other words, the effect of suction is to increase the local

Nusselt number. Due to mass suction, the fluid is brought closer to the surface and consequently it prevents the vorticity diffusion. Further, the thickness of the thermal boundary layer for upper solution branch is lower than the same thickness of the lower solution branch. The effect of the stretching/shrinking parameter in the shrinking sheet case on the velocity profile and the temperature distribution is demonstrated in Fig. 11. The results show that the velocity and the thermal boundary layers' thicknesses increase as the velocity ratio parameter enhances in the shrinking-sheet case. Finally, it can be observed that the far field boundary conditions (Eq. (10)) are all satisfied asymptotically. Thus, it is extra support for the validity of the exact solution results obtained and the existence of the dual solutions given in the figures of this section.

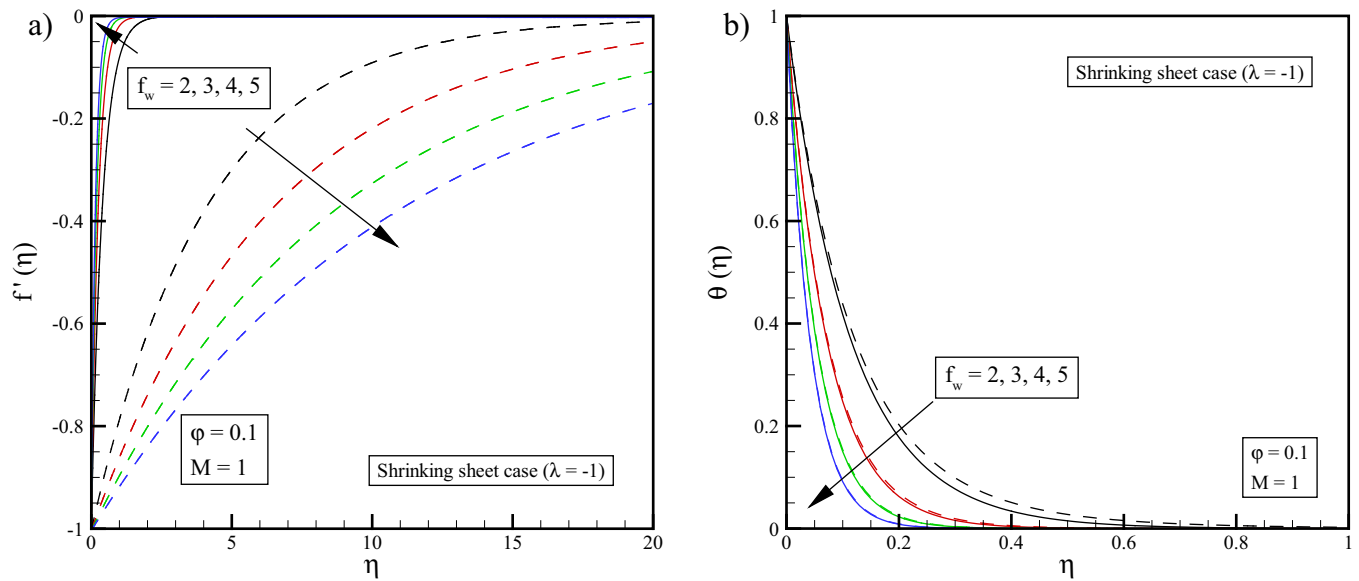


Fig. 10. Effect of the mass suction/injection parameter on (a) the velocity profile and (b) the temperature distribution; the solid line corresponds to the upper branch solution and the dashed line denotes to the lower branch solution.

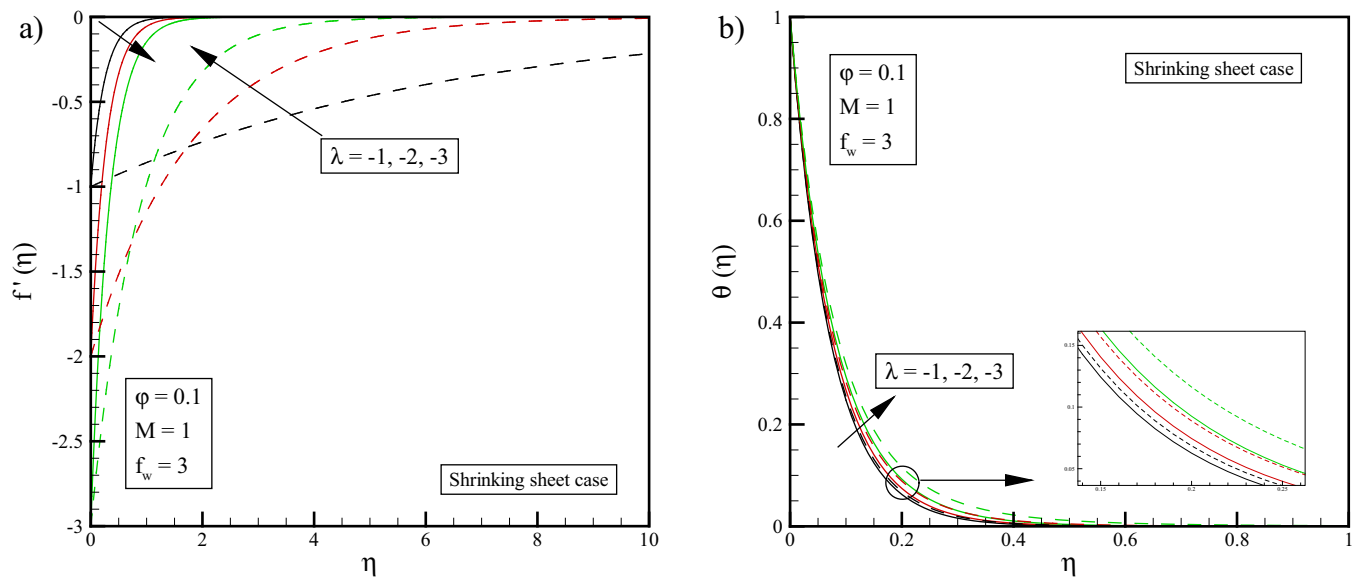


Fig. 11. Effect of the stretching/shrinking parameter on (a) the velocity profile and (b) the temperature distribution; the solid line corresponds to the upper branch solution and the dashed line denotes to the lower branch solution.

5.3. Physical quantities of interest

The effects of the different involved parameters including the nanoparticle volume fraction parameter, the magnetic parameter, the mass suction/injection parameter, and the stretching/shrinking parameter for both the stretching and shrinking-sheet cases on the dimensionless skin friction coefficient and the Nusselt number are displayed in Figs. 12–15. The lower branch solution results for the shrinking-sheet case are presented using the star symbol lines. The magnitude of the dimensionless skin friction coefficient increases for increasing values of nanoparticle volume fraction parameter, the magnetic parameter, the stretching/shrinking parameter, the mass suction/injection parameter (in the suction mode) for the

stretching-sheet case. The results show that the dimensionless Nusselt number increases by increasing the values of nanoparticle volume fraction parameter, the stretching/shrinking parameter (in the stretching-sheet case), and the mass suction/injection parameter (in the suction mode) and also decreasing the magnetic parameter. The effect of nanoparticle type variations on the dimensionless skin friction coefficient and local Nusselt number for both the stretching and shrinking-sheet cases is demonstrated in Fig. 16. In Table 1, it is presented that Cu and Al_2O_3 have the highest and lowest density values, respectively, among the different types of nanoparticles considered. Hence, by considering Al_2O_3 leads to the minimum amount of skin friction coefficient absolute value, while choosing Cu gives the maximum value. The

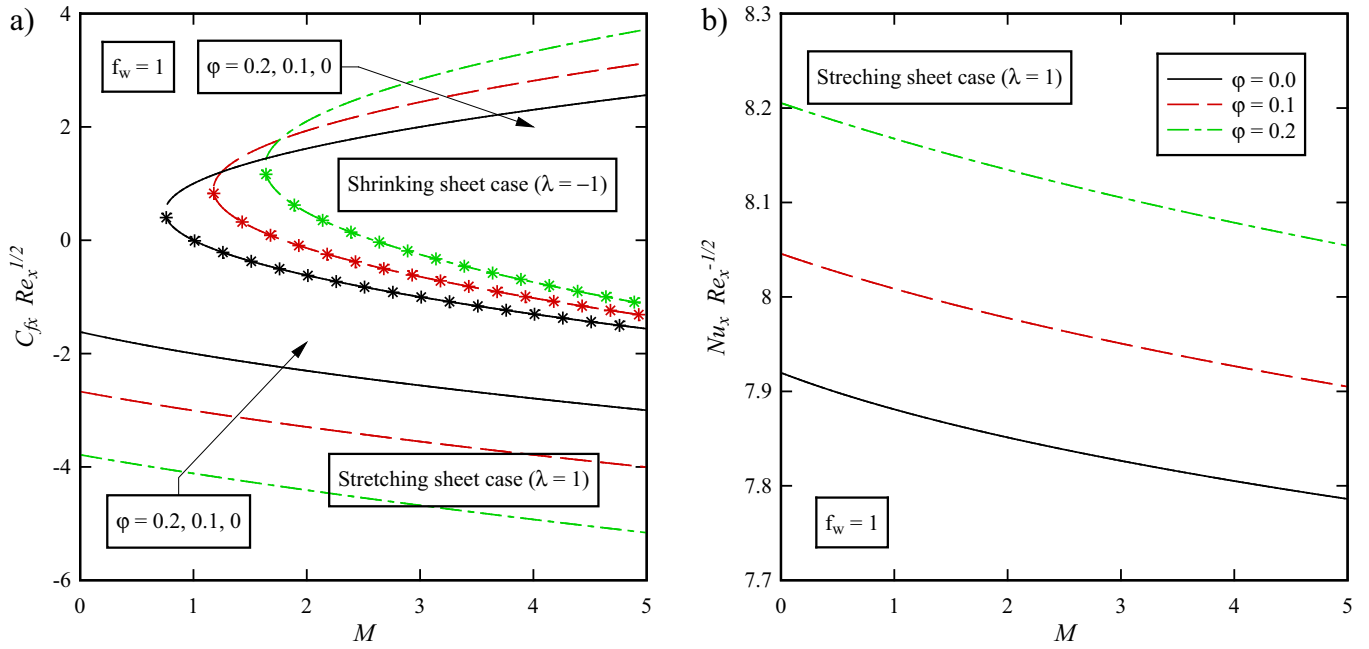


Fig. 12. The variations of the dimensionless (a) skin friction coefficient and (b) Nusselt number for different values of nanoparticle volume fraction parameter for a wide range of magnetic parameter for both the stretching and shrinking sheet cases.

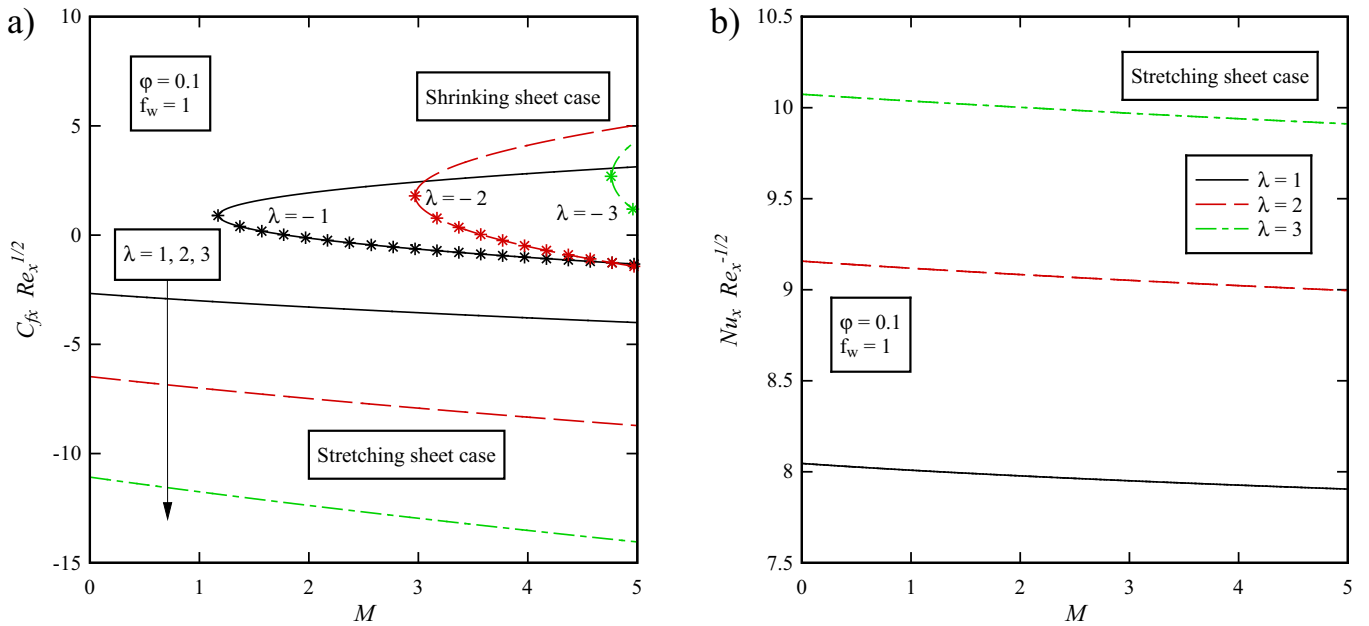


Fig. 13. The variations of the dimensionless (a) skin friction coefficient and (b) Nusselt number for different values of the stretching/shrinking parameter for a wide range of the magnetic parameter for both the stretching and shrinking sheet cases.

current-mentioned trend of the skin friction coefficient applies for both the stretching and shrinking-sheet cases. Further, the copper nanoparticle has the largest local Nusselt number because of its higher thermal conductivity value among the other nanoparticles. In addition, the lowest heat transfer rate is obtained for the TiO_2 nanoparticle due to domination of conduction mode of heat transfer and because of its lowest thermal conductivity compared to the other nanoparticles. This behavior is similar to that reported by Freidoonimehr et al. [7]. The results illustrate this fact that the

nanoparticle type is an important factor in the cooling and heating processes.

According to Fig. 12, in the stretching sheet case ($\lambda = 1$) and in the presence of a constant magnetic field, the skin friction decreases as the number of nanoparticles increase. This happens due to the polarization of nanoparticles and reduced adhesiveness coefficient. It is also clear that skin friction coefficient decreases as the magnetic field grows in size which enhances the polarization of the nanoparticles.

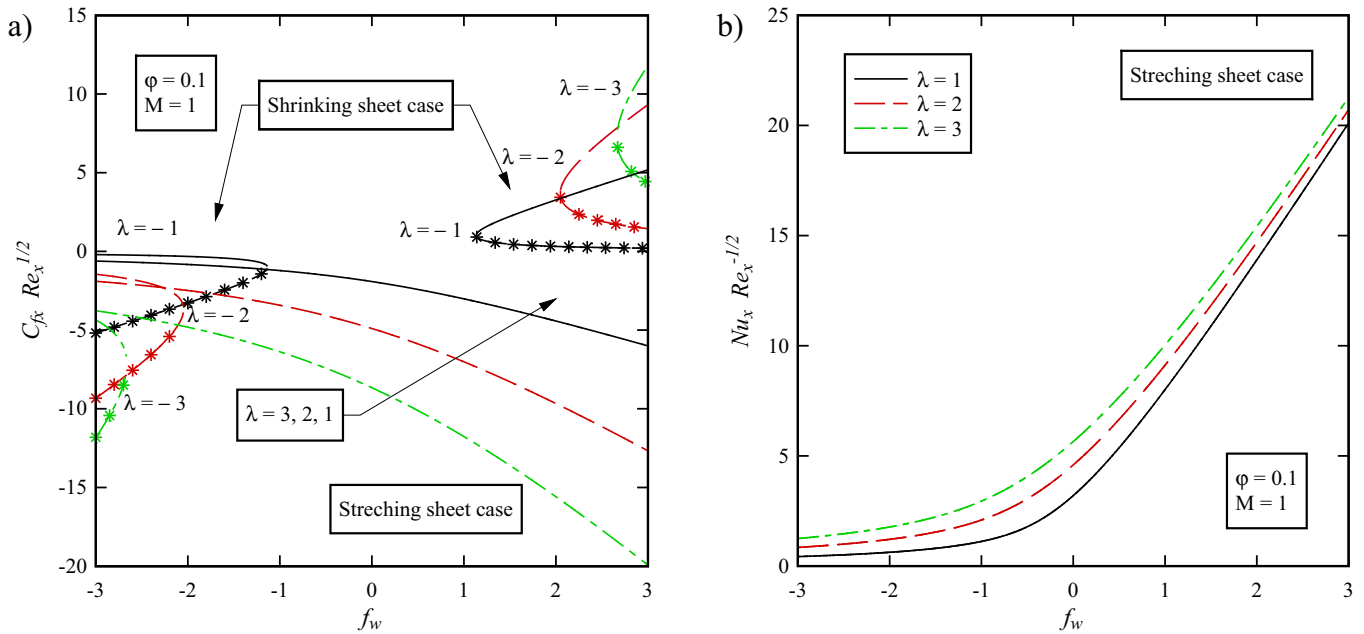


Fig. 14. The variations of the dimensionless (a) skin friction coefficient and (b) Nusselt number for different values of the stretching/shrinking parameter for a wide range of the mass suction/injection parameter for both the stretching and shrinking sheet cases.

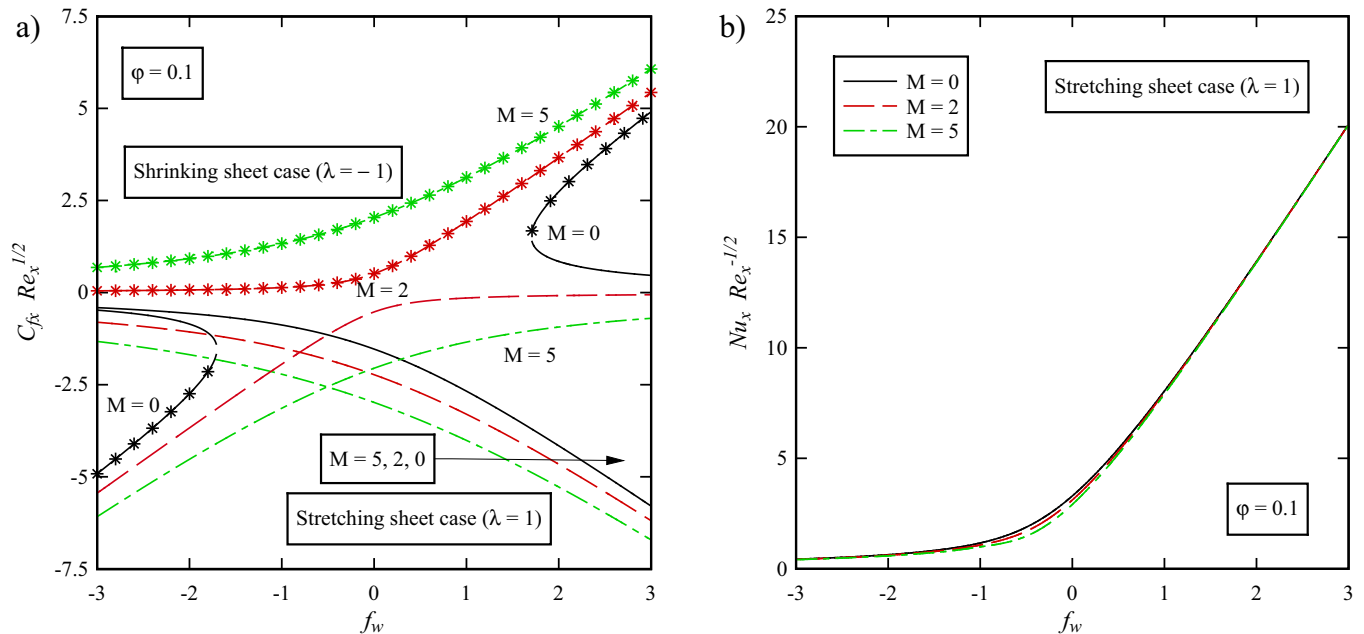


Fig. 15. The variations of the dimensionless (a) skin friction coefficient and (b) Nusselt number for different values of the magnetic parameter for a wide range of the mass suction/injection parameter for both the stretching and shrinking sheet cases.

Fig. 13 shows that in the case of a positive λ , the value of skin friction coefficient decreases by increasing λ because of a higher flow rate which makes velocity in the boundary layer to increase dramatically and consequently the skin friction coefficient to decrease. For all values of λ , a more powerful magnetic field and a higher polarization of the nanoparticles do not affect this trend, though with a negative λ the change in flow direction would cause higher changes in the velocity and skin friction coefficient, consequently.

As it can be seen in Fig. 14, the mass of suction/injection in the boundary layer, increases the velocity changes. This increment in velocity change, decreases skin friction coefficient. On the other hand, whenever the mass of suction/injection to the boundary layer increases, the skin friction coefficient decreases. Also by increasing in the mass of suction/injection, the Nusselt number is enhanced. The Nusselt number, in all λ values, trend to same amount with increasing of the mass suction/injection parameter. Domination of

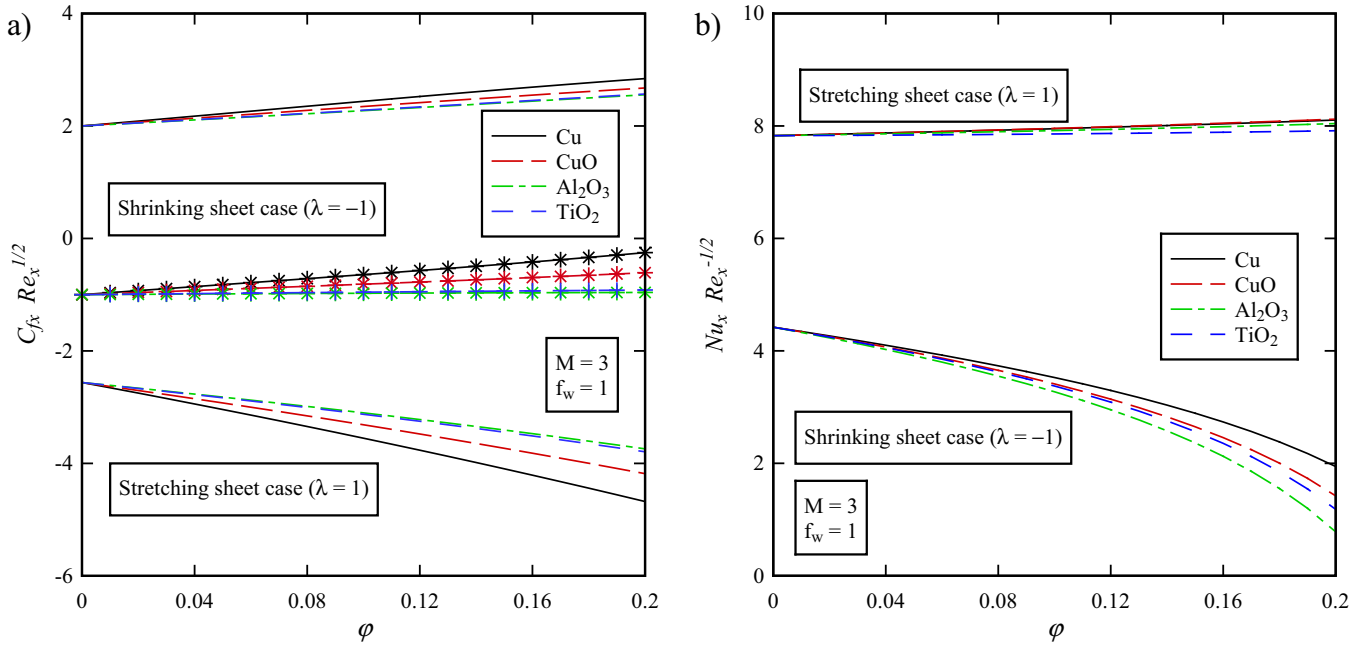


Fig. 16. The variations of the dimensionless (a) skin friction coefficient and (b) Nusselt number for different type of nanoparticles for a wide range of nanoparticle volume fraction parameter for both the stretching and shrinking sheet cases.

conduction heat transfer to convection heat transfer is the cause of this phenomenon.

As it can be found in Fig. 15, the increment of the suction/injection parameter and the magnetic parameter will change due to enhancement in velocity changes. As a result for the positive values of λ , the skin friction coefficient decreases and for the negative values of λ , the skin friction coefficient increases. Therefore, as it can be seen in Fig. 15(b), the magnetic field has less meaningful effect on the value of the Nusselt number than the mass suction/injection parameter does. This reveals that the mass of suction/injection parameter is a dominate parameter in heat transfer.

Fig. 16 indicates that by increasing the molecular weight and decreasing the thermal conductivity of the nanoparticles, the amount of skin friction coefficient in terms of the nanoparticle volume fraction increases. Also, for different types of nanoparticles, the Nusselt number decreases with a wide range of volume fraction. Generally, it can be concluded that the mass suction/injection parameter is a dominant effective parameter on the heat transfer.

The variations of the averaged entropy generation number for different values of the magnetic parameter (M), the stretching/shrinking parameter (λ), the mass suction/injection parameter (f_w), the Reynolds number (Re), the Brinkman number (Br), the Hartmann number (Ha), as well as different types of nanoparticles (Cu, CuO, Al_2O_3, TiO_2) for a wide range of the nanoparticle volume fraction parameter (ϕ) are displayed in Fig. 17. The results illustrate that increasing in the values of the nanoparticle volume fraction parameter, the magnetic parameter, the mass suction/injection parameter, the Reynolds number, the Brinkman number, and the Hartmann number or decreasing the stretching/shrinking parameter causes an increase in the entropy generation number. The entropy generation due to irreversibilities of heat transfer and fluid friction and consequently the averaged entropy generation number increase with an increase in the Reynolds number can be inferred from Eq. (31). Further, an increase in the entropy generation due to the fluid friction and joule dissipation irreversibilities occurs with increasing the value of the Brinkman

number. In addition, joule dissipation irreversibility and the averaged entropy generation number are the increasing functions of the Hartmann number. It is also clear that the copper nanoparticle has the largest averaged entropy generation number and the aluminum oxide has the lowest one.

6. Conclusions

In the current perusal, the problem of fluid flow and heat transfer have been studied for the steady, laminar, nanofluid flow induced by a stretching/shrinking-sheet considering transpiration effect. Four different water based nanofluids containing $TiO_2, Al_2O_3, Cu,$ and CuO nanoparticles have been considered in the analysis. Exact solutions for the velocity and the temperature distributions have been developed and discussed. The results show that in the shrinking sheet case the lower solution branch for the velocity and temperature profiles demonstrate a larger boundary layer thickness compared to the upper solution branches. Entropy generation equation has been derived as a function of the velocity and the temperature gradients. The influences of the seven key thermo-physical parameters governing the flow i.e. the nanoparticle volume fraction parameter, the magnetic parameter, the mass suction/injection parameter, the stretching/shrinking parameter, the Reynolds number, the Brinkman number, and the Hartmann number on the velocity and the temperature distributions, the skin friction coefficient, the local Nusselt number, and the averaged entropy generation number have been presented graphically and interpreted in details. The main findings of this study can be summarized as follows:

- Entropy generation number increases with increasing the values of nanoparticle volume fraction parameter, the magnetic parameter, the mass suction/injection parameter, the Reynolds number, the Brinkman number, and the Hartmann number.
- Entropy generation number can be reduced through the increase of stretching/shrinking parameter.

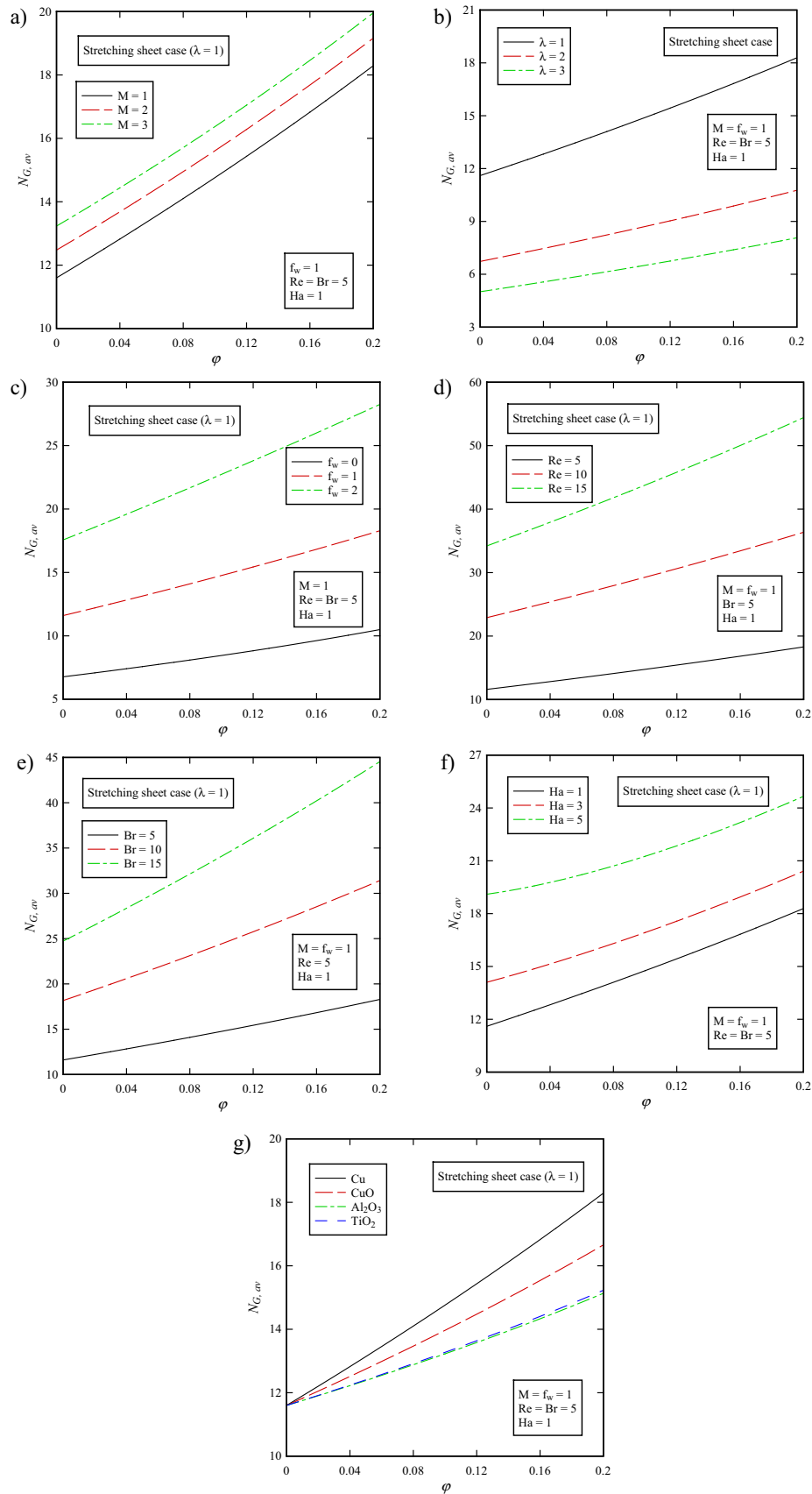


Fig. 17. The variations of the averaged entropy generation number for different values of (a) the magnetic parameter, (b) the stretching/shrinking parameter, (c) the mass suction/injection parameter, (d) the Reynolds number, (e) the Brinkman number, (f) the Hartmann number, and (g) type of nanoparticles for a wide range of nanoparticle volume fraction parameter.

- Using copper nanoparticles leads to the maximum entropy generation while aluminum oxide nanoparticles minimize the entropy generation number.
- Suction/injection parameter is more effective in the value of Nusselt number compared to the magnetic field parameter.
- By increasing the molecular weight and decreasing the thermal conductivity of the nanoparticles, the amount of skin friction coefficient in terms of the nanoparticle volume fraction increases.
- For different types of nanoparticles, the Nusselt number declines with a wide range of volume fraction.
- Mass suction/injection parameter is the dominant effective parameter on the heat transfer.

Acknowledgement

This work has been financially supported by the office of research and development of Ferdowsi University of Mashhad under contract number 2/40626.

References

- [1] S.U.S. Choi, J.A. Eastman, Enhancing thermal conductivity of fluids with nanoparticles, *Mater. Sci.* 231 (1995) 99–105.
- [2] J.A. Eastman, U.S. Choi, S. Li, G. Soyes, L.J. Thompson, R.J. DiMelfi, Novel thermal properties of nanostructured materials, *Mater. Sci. Forum* 312–314 (1999) 629–634.
- [3] Y. Xuana, W. Roetzel, Conceptions for heat transfer correlation of nanofluids, *Int. J. Heat Mass Transf.* 43 (2000) 3701–3707.
- [4] H. Masuda, A. Ebata, K. Teramae, H. Hishinuma, Alteration of thermal conductivity and viscosity of liquid by dispersing ultra-fine particles. Dispersion of 7–Al₂O₃, SiO₂ and TiO₂ ultra-fine particles, *Netsu Bussei* 4 (1993) 227–233.
- [5] Y. Xuan, Q. Li, Investigation on convective heat transfer and flow features of nanofluids, *J. Heat Transf.* 125 (2003) 151–155.
- [6] M.M. Rashidi, A. Hosseini, I. Pop, S. Kumar, N. Freidoonimehr, Comparative numerical study of single and two-phase models of nanofluid heat transfer in wavy channel, *Appl. Math. Mech.* 35 (2014) 831–848.
- [7] N. Freidoonimehr, M.M. Rashidi, S. Mahmud, Unsteady MHD free convective flow past a permeable stretching vertical surface in a nanofluid, *Int. J. Therm. Sci.* 87 (2015) 136–145.
- [8] N. Freidoonimehr, B. Rostami, M.M. Rashidi, E. Momoniati, Analytical modelling of three-dimensional squeezing nanofluid flow in a rotating channel on a lower stretching porous wall, *Math. Probl. Eng.* 2014 (2014) 14.
- [9] Navid Freidoonimehr, M.M. Rashidi, Dual solutions for MHD jeffery-hamel nanofluid flow in non-parallel walls using predictor homotopy analysis method, *J. Appl. Fluid Mech.* 8 (2015) 911–919.
- [10] N. Freidoonimehr, B. Rostami, M.M. Rashidi, Predictor homotopy analysis method for nanofluid flow through expanding or contracting gaps with permeable walls, *Int. J. Biomath.* 08 (2015) 1550050.
- [11] A. Malvandi, F. Hedayati, D.D. Ganji, Thermodynamic optimization of fluid flow over an isothermal moving plate, *Alexandria Eng. J.* 52 (2013) 277–283.
- [12] A. Bejan, *Entropy Generation Minimization: the Method of Thermodynamic Optimization of Finite-Size Systems and Finite-Time Processes*, CRC Press, 1996.
- [13] A. Bejan, *Second-law analysis in heat transfer and thermal design*. *Advances in Heat Transfer*, Elsevier, vol. 15, 1982, pp. 1–58.
- [14] O. Mahian, S. Mahmud, S.Z. Heris, Analysis of entropy generation between co-rotating cylinders using nanofluids, *Energy* 44 (2012) 438–446.
- [15] A. Bejan, Second law analysis in heat transfer, *Energy* 5 (1980) 720–732.
- [16] H.F. Oztop, K. Al-Salem, A review on entropy generation in natural and mixed convection heat transfer for energy systems, *Renew. Sustain. Energy Rev.* 16 (2012) 911–920.
- [17] S. Aiboud, S. Saouli, Second law analysis of viscoelastic fluid over a stretching sheet subject to a transverse magnetic field with heat and mass transfer, *Entropy* 12 (2010) 1867–1884.
- [18] M.M. Rashidi, M. Ali, N. Freidoonimehr, F. Nazari, Parametric analysis and optimization of entropy generation in unsteady MHD flow over a stretching rotating disk using artificial neural network and particle swarm optimization algorithm, *Energy* 55 (2013) 497–510.
- [19] M.M. Rashidi, S. Abelman, N. Freidoonimehr, Entropy generation in steady MHD flow due to a rotating porous disk in a nanofluid, *Int. J. Heat Mass Transf.* 62 (2013) 515–525.
- [20] M.H. Abolbashari, N. Freidoonimehr, F. Nazari, M.M. Rashidi, Entropy analysis for an unsteady MHD flow past a stretching permeable surface in nanofluid, *Powder Technol.* 267 (2014) 256–267.
- [21] M.H. Abolbashari, N. Freidoonimehr, F. Nazari, M.M. Rashidi, Analytical modeling of entropy generation for Casson nanofluid flow induced by a stretching surface, *Adv. Powder Technol.* 26 (2015) 542–552.
- [22] S. Jafari, N. Freidoonimehr, Second law of thermodynamics analysis of hydro-magnetic nanofluid slip flow over a stretching permeable surface, *J. Braz. Soc. Mech. Sci. Eng.* (2014) 1–12.
- [23] M.M. Rashidi, S. Mahmud, N. Freidoonimehr, B. Rostami, Analysis of entropy generation in an MHD flow over a rotating porous disk with variable physical properties, *Int. J. Exergy* 16 (2015) 481–503.
- [24] M.M. Rashidi, S. Bagheri, E. Momoniati, N. Freidoonimehr, Entropy analysis of convective MHD flow of third grade non-Newtonian fluid over a stretching sheet, *Ain Shams Eng. J.*, in press.
- [25] H.C. Brinkman, The viscosity of concentrated suspensions and solutions, *J. Chem. Phys.* 20 (1952) 571.
- [26] H. Oztop, E. Abu-Nada, Numerical study of natural convection in partially heated rectangular enclosures filled with nanofluids, *Int. J. Heat Fluid Flow* 29 (2008) 1326–1336.
- [27] <http://www.mhtl.uwaterloo.ca/>. Retrieved 12/03/2016.
- [28] M. Turkyilmazoglu, Multiple solutions of heat and mass transfer of MHD slip flow for the viscoelastic fluid over a stretching sheet, *Int. J. Therm. Sci.* 50 (2011) 2264–2276.
- [29] M. Turkyilmazoglu, Exact solutions for two-dimensional laminar flow over a continuously stretching or shrinking sheet in an electrically conducting quiescent couple stress fluid, *Int. J. Heat Mass Transf.* 72 (2014) 1–8.
- [30] M. Turkyilmazoglu, Heat and mass transfer of MHD second order slip flow, *Comput. Fluids* 71 (2013) 426–434.